Reinforcing neuron extraction and spike inference in calcium imaging using deep self-supervised learning

Xinyang Li[1,2,3†], Guoxun Zhang[1,3†], Jiamin Wu[1,3], Yuanlong Zhang[1,3], Zhifeng Zhao[1,3],

Xing Lin[1,3,4], Hui Qiao[1,3], Hao Xie[1,3], Haoqian Wang[2,3*], Lu Fang[3,5*] & Qionghai Dai[1,3*]

[1]*Department of Automation, Tsinghua University, Beijing 100084, China*

[2]*Tsinghua Shenzhen International Graduate School, Tsinghua University, Shenzhen, 518055, China*

[3]*Institute for Brain and Cognitive Science, Tsinghua University, Beijing 100084, China.*

[4]*Beijing Innovation Center for Future Chips, Tsinghua University, Beijing 100084, China*

[5]*Department of Electronic Engineering, Tsinghua University, Beijing 100084, China*

[†]*These authors contributed equally to this work.*

*Correspondence: wanghaoqian@tsinghua.edu.cn; fanglu@tsinghua.edu.cn; qhdai@mail.tsinghua.edu.cn

ABSTRACT

Calcium imaging is inherently susceptible to detection noise especially when imaging with high frame rate or under low excitation dosage. We developed DeepCAD, a self-supervised learning method for spatiotemporal enhancement of calcium imaging without requiring any high signal-to-noise ratio (SNR) observations. Using this method, detection noise can be effectively suppressed and the imaging SNR can be improved more than tenfold, which massively improves the accuracy of neuron extraction and spike inference and facilitate the functional analysis of neural circuits.

Calcium imaging enables parallel recordings of large neuronal ensembles in living animals[1-4] and offers a new possibility for deciphering information propagation, integration, and computation in neural circuits[5]. To obtain accurate neuron extraction and spike inference for downstream neuroscience analysis, high-SNR calcium imaging is desired. However, due to the paucity of fluorescence photons caused by low peak accumulations and fast dynamics of *in vivo* calcium transients[6,7], calcium imaging is easy to be contaminated by detection noise (*i.e.* photon shot noise and electronic noise), especially in functional imaging where high temporal resolution is particularly important for analyzing neural activities[8].

To capture sufficient fluorescence photons for high-SNR calcium imaging, the most direct way is to use high excitation dosage, but concurrent photobleaching, phototoxicity[9,10], and tissue heating[11] are detrimental for sample health and photosensitive biological processes, which limits the maximal excitation power for long-term *in vivo* imaging[12]. More effective

35   strategies include using brighter calcium indicators[7,13] and more sensitive photoelectric

36   detectors[14], but their performances are still largely restricted in photon-limited conditions such

37   as dendritic imaging and deep-tissue imaging. Apart from these physical or biological

38   approaches, data-driven methods are promising to offer an alternative solution to recover

39   faithful signals from degraded recordings and reduce the photon budget of calcium imaging.

40   As an intelligent signal processing technique, deep learning has been adopted by microscopists

41   and achieved impressive performance in fluorescence imaging[15-18]. However, calcium

42   transients are highly dynamic, non-repetitive activities and a firing pattern cannot be

43   captured twice. Previous schemes for obtaining ground-truth images (*i.e.* clean images

44   without noise contamination or high-SNR images with the same underlying scene) by

45   extending integration time or averaging multiple noisy frames are no longer feasible,

46   posing an entrenched obstacle for conventional supervised learning methods.

47   In this paper, we present DeepCAD, a self-supervised learning method for calcium imaging

48   denoising by over tenfold SNR improvement without requiring any high-SNR observations for

49   training. DeepCAD is based on the insight that a deep neural network can converge to a mean

50   estimator even the target image used for training is another corrupted sampling of the same

51   scene[19]. When looking at calcium imaging data, we explored the temporal redundancy of

52   pervasive video-rate imaging and found that any two consecutive frames can be regarded as

53   two independent samplings of the same underlying firing pattern, which can be used for

54   training of denoising models. Furthermore, the input and output data are designed to be

55   3D volumes rather than 2D frames to fully exploit spatiotemporal information in the

56   time-lapse stack. We show that such a 3D self-supervised method is extremely effective for

57   calcium imaging denoising and even the subtlest calcium fluctuations induced by a single

58   action potential (AP) can be restored from severely corrupted images. Finally, a Fiji-based

59   plugin along with a pre-trained model were released to make our method easy to access and

60   convenient to use.

61   The general principle of DeepCAD is schematized in Fig. 1a. For network architecture, we

62   employed 3D U-Net[20] to aggregate spatiotemporal information in multiple frames using

63   3D convolutional layers (Supplementary Fig. 1, Methods), which endows DeepCAD with

64   better denoising capability than 2D architecture or classical methods (Supplementary Fig. 2).

65   Benefiting from the self-supervised strategy, a single low-SNR stack of ~3500 frames is

66   sufficient to be a complete training set. To generate the training set, two sub-stacks consisting

67   of interlaced frames were split from the original low-SNR stack and 3D tiles were extracted

68   from these sub-stacks for training (Supplementary Fig. 3). They contain approximate identical

69   calcium transients when the original stack was imaged at near video rate, which is common for

70   commercial or customized microscopes. After proper training, interpretable features can be

71   learned (Supplementary Fig. 4) and the model can be applied to subsequent acquisitions

72   without extra training (Fig. 1b). Although the network was trained on specified spatial and

73   temporal resolution, we found that it had non-inferior performance on various frame rates

74   (Supplementary Fig. 5) and magnifications (Supplementary Fig. 6), indicating the great

75   scalability and generalization for versatile applications of DeepCAD.

76   To quantitatively evaluate the performance of DeepCAD, we first validated it on simulated

77   calcium imaging data of different imaging SNRs (Supplementary Figs. 7-8 and Supplementary

78   Notes 1-2), which contains synchronous noise-free recordings as the ground truth for

79   comparison. The constrained nonnegative matrix factorization (CNMF) algorithm[21] was

80   used for downstream neuron extractions (Methods). After the enhancement of

81   DeepCAD, more active neurons can be detected, especially when imaging SNR is low

82   (Fig. 1c). The accuracy of neuron extraction was also quantified with F1 score and

83   significant improvement was observed across a wide range of intersection-over-union (IoU)

84   thresholds (Fig. 1d,e). For a typical IoU threshold of 0.7, the segmentation accuracy was

85   improved by 2.4 folds (0.84 contrast to 0.35). Benefiting from the improved imaging

86   quality, calcium traces extracted from the denoised data possess higher fidelity. To

87   investigate the temporal enhancement of DeepCAD, we extracted calcium traces of all

88   neurons from both raw noisy data and the enhanced counterpart. The Pearson

89   correlation with the clean traces was significantly improved after denoising (Fig. 1f).

90   Even the slightest calcium transients can be restored from the original noisy data (Fig.

91   1g and Supplementary Fig. 9). These facts suggest that the spatiotemporal enhancement

92   of DeepCAD can improve the accuracy of neuronal localization and trace extraction

93   and largely facilitate the analysis of neural circuits.

94   To verify the effectiveness and reliability of DeepCAD on neuroscience research, we then

95   demonstrated its performance on two-photon calcium imaging based on data released by

96   Svoboda lab[7]. In this dataset, simultaneous cell-attached electrophysiological recordings (Fig.

97   2a) are synchronized with two-photon imaging and serve as the reference of calcium transients

98   and the ground truth of spike inference. Contaminated by detection noise, both the spatial

99   footprint and temporal traces of the neuron were severely corrupted in the original data (Fig.

100   2b). After we applied DeepCAD to enhance these data, the annular cytoplasm became

101   recognizable and calcium traces were liberated from noise (Fig. 2c and Supplementary Video

102   1). Even the most imperceptible calcium transients evoked by one AP, two APs, and three APs

103   were clearly distinguished and still maintain their original dynamics (Fig. 2d-g), which

104   otherwise would be submerged in noise. For further comparison, we extracted single-pixel

105   fluorescence from cytoplasmic pixels and found that calcium transients can be unveiled at a

106   single-pixel scale (Supplementary Fig. 10). Moreover, we performed spike inference (Methods)

107   on traces extracted from the original data as well as the corresponding denoised data. Owing to

108   the improvement of imaging SNR, the error rate of spike inference was consequently decreased

109   (Fig. 2h and Supplementary Fig. 11). Among 107 independent calcium traces, 86% of them

110   were observed to have lower error rates.

111   Next, we employed DeepCAD for noise removal of calcium imaging of large neuronal

112   populations in awake mice. To obtain high-SNR recordings for validation of our method, we

113   designed and built a two-photon imaging system with the capability of simultaneous low-SNR

114   and high-SNR recording (Supplementary Fig. 12 and Methods). The high-SNR detection path

115   was strictly synchronized with the low-SNR detection path but with about 10-fold higher

116   imaging SNR (Supplementary Fig. 13), which can be used as the reference for our denoising

117   results. We first imaged spontaneous neuropil activities in cortical layer 1 of a transgenic mouse

118   expressing GCaMP6f and found that calcium fluctuations indiscernible in original low-SNR

119   recordings can be effectively recovered by DeepCAD (Fig. 3a-c and Supplementary Video 2).

120   The imaging SNR was improved more than 10 folds considering that the SNR of enhanced

121   recordings even surpasses corresponding high-SNR reference. Fluorescence traces of dendritic

122   pixels can be accurately resolved and keep high consistency with the high-SNR reference (Fig.

123   3d-e and Supplementary Fig. 14). We also applied DeepCAD to enhance calcium imaging of

124   somatic signals. After denoising, neuronal distribution and circuit dynamics can be recognized

125   from a single frame (Fig. 3f-h and Supplementary Video 3). Using CNMF as the downstream

126   source extraction method, 52.6% (229 contrast to 150) more active neurons can be extracted

127   (Fig. 3i,j and Supplementary Fig. 15) and the trace peak SNR of extracted neurons was also

128   improved more than two folds (9.9 contrast to 4.8, median value) (Fig. 3k), indicating that the

129   functional analysis of large neuronal populations can be effectively strengthened due to

130   improved SNR.

131   In summary, we demonstrate DeepCAD, a deep self-supervised learning-based method for

132   spatiotemporal enhancement of calcium imaging. Quantitative evaluation on both simulated

133   and experimental data shows that the accuracy of neuron extraction and spike inference can be

134   largely reinforced after denoising. To fully evaluate the capability and reliability of our method,

135   a customized two-photon microscope was built to capture synchronized low-SNR and high-

136   SNR recordings, which indicates that DeepCAD enables a more than tenfold improvement in

137   imaging SNR. To maximize its accessibility, we released an open-source Fiji plugin

138   (Supplementary Fig. 16 and Supplementary Notes 3) and a pre-trained DeepCAD model for

139   two-photon imaging of neuron populations. Our method can be efficiently configured on a

140   common desktop and achieve comparable performance on different imaging systems

141   regardless of objectives and detectors (Supplementary Fig. 17 and Supplementary Video 4).

142   Although DeepCAD is currently investigated only on two-photon microscopy, it can be easily

143   extended to other imaging modalities such as wide-field microscopy and light-sheet

144   microscopy. We anticipate that this method could serve as a general processing step for calcium

145   imaging in photon-limited conditions and promote long-term and high-fidelity recording of

146   neural activities.

Methods

Optical setup. A two-photon imaging system was designed to capture strictly synchronized low-SNR and high-SNR calcium recordings for validation of our method. Our system was based on a standard two-photon laser scanning microscope (2PLSM) and the detection path was specially designed to split the fluorescence in a ratio of 1:10. All components of our imaging system are commercially available or easy to fabricate. The schematic of the custom-built two-photon microscope is shown in Supplementary Fig. 12. At the forefront of the optical path, a titanium-sapphire laser system with tunable wavelength (Mai Tai HP, Spectra-Physics) was used as the illumination source to emit the linearly polarized, femtosecond-pulsed Gaussian excitation beam (920 nm central wavelength, pulse width <100 fs, 80 MHz repetition rate). A half-wave plate (AQWP10M-980, Thorlabs) was used to adjust the polarization of the laser beam. Then the laser beam went through an electro-optic modulator (350-80LA-02, Conoptics) to modulate the excitation power and the half-wave plate was rotated to make the electro-optic modulator have maximal extinction ratio. A 4f system composed of two achromatic lenses (AC508-200-B, Thorlabs) with the same focal length was followed to collimate the laser beam. Another 4f system (AC508-100-B and AC508-400-B, Thorlabs) with a fourfold magnification was used to expand the laser beam and guide the beam into a galvo-resonant scanner (8315K/CRS8K, Cambridge Technology) for fast optical scanning. The scanner mount was optimally designed for reliable and distortion-free scanning. Then the beam went through a scan lens (SL50-2P2, Thorlabs)

168   and a tube lens (TTL200MP, Thorlabs) and converged into a tight focus through a high

169   numerical aperture (NA) water-dipping objective (25×/1.05 NA, XLPLN25XWMP2,

170   Olympus). A high-precision piezo actuator (P-725, Physik Instrumente) was

171   additionally used to drive the objective for fast axial scanning. The beam size at the

172   back aperture of the objective was further restricted with an iris set behind the beam

173   expander (L4) to keep the back aperture of the objective underfilled. The effective

174   excitation NA was about 0.5 in our imaging experiments.

175   For the detection path, fluorescence excited by the Gaussian focus was first

176   collected by the objective. High-NA detection is helpful to detect more fluorescence

177   photons and improve the signal intensity. A long-pass dichroic mirror (DMLP650L,

178   Thorlabs) was used to separate fluorescence by reflecting the fluorescence signals and

179   transmitting the excitation light. A 1:9 (reflectance: Transmission) non-polarizing plate

180   beam splitter (BSN10, Thorlabs) was then placed in the detection path. All fluorescence

181   going through the beam splitter will be split into a 10% component (low-SNR path) and

182   a 90% component (high-SNR path), propagating in two orthogonal directions and

183   detected by two photomultiplier tubes (PMT1001, Thorlabs). A pair of fluorescence

184   filters (MF525-39, Thorlabs; ET510/80M, Chroma) was configured in front of each

185   PMT to fully block wavelengths outside the emission passband of green fluorescent

186   protein (GFP). To improve detection efficiency, we conjugated the back aperture of the

187   objective to the sensor planes of the two PMTs using two 4f systems (TTL200-A and

188   AC254-050-A, Thorlabs). The two detection paths recorded synchronized fluorescence

189   signals but with quite different imaging SNR. Although the high-SNR recording still

190   suffers from noise, it can be used as the reference to identify underlying structures and

191   calcium fluctuations. The field-of-view (FOV) of our two-photon imaging system is

192   about 600 μm and the frame rate is about 30 Hz.

193   **System calibration.** To confirm the fluorescence intensity ratio between the high-SNR

194   detection path and the low-SNR detection path, we imaged 1 μm green-fluorescent

195   beads (G0100, ThermoFisher) for system calibration. The beads suspension was first

196   diluted and embedded in 1.0% agarose and then mounted on a microscope slide to form

197   a single beads layer composed of sparse beads. A specified region was continuously

198   scanned to acquire 500 consecutive frames. These frames can be regarded as

199   independent samplings of the same underlying scene. To reduce the impact of detection

200   noise, we averaged these frames to obtain the noise-free image of each path

201   (Supplementary Fig. 13). All beads in the FOV were manually segmented and the

202   intensity of each bead was calculated by averaging all pixels inside its segmentation

203   mask. According to our statistical analysis, the fluorescence intensity of the high-SNR

204   detection path was approximately tenfold higher than that of the low-SNR detection

205   path.

206   **Mouse preparation and calcium imaging.** All experiments involving mice were

207   performed in accordance with institutional guidelines for animal welfare and have been

208   approved by the Institutional Animal Care and Use Committee (IACUC) of Tsinghua

209   University.

210   Adult transgenic mice (Ai148D/Rasgrf2-dCre) at 8-12 postnatal weeks were

211   anesthetized with 1.5% isoflurane and craniotomy surgeries were conducted using a

212   stereotaxic instrument (68018, RWD Life Science) under a bright-field binocular

213   microscope (77001S, RWD Life Science). A custom-made coverslip fitting the shape

214   of the cranial window (~6 mm in diameter) was embedded and cemented to the skull.

215   A biocompatible titanium headpost was then cemented to the skull for stable head

216   fixation. The edge of the cranial window was enclosed with dental cement to hold the

217   immersion water of the objective. After the surgery, 0.25mg/g body weight of

218   Trimethoprim (TMP) was intraperitoneally injected to induce the expression of

219   GCaMP6f genetically encoded calcium indicator (GECI) in layer 2/3 neurons across

220   the whole brain. To reduce potential inflammation, 5 mg/kg body weight of Ketoprofen

221   was injected subcutaneously. Each mouse was housed in a separate cage for 1-2 weeks

222   of postoperative recovery.

223   Imaging experiments were carried out when the cranial window became clear and

224   no inflammation occurred. Mice were first rapidly anesthetized with 3.0% isoflurane

225   and then fixed onto a custom-made holder with the headpost. The mouse holder was

226   mounted on a precision translation stage with three motorized axes (M-VP-25XA-

227   XYZL, Newport) to find the region of interest (ROI) for imaging. The correction ring

228   of the objective was adjusted to compensate for the coverslip thickness and eliminate

229   spherical aberrations. The excitation power after the objective was kept below 140 mW

230   in all experiments to avoid potential laser-induced tissue damage. Gaseous anesthesia

231   was switch off and the mice kept awake during the whole imaging process.

232   **Network architecture and training details.** The network architecture of DeepCAD

233   employs 3D U-Net, which is reported to have superior performance on the segmentation

234   of volumetric data[20]. In general, the network is composed of a 3D encoder module (the

235   contracting path), a 3D decoder module (the expanding path), and three skip

236   connections from the encoder module to the decoder module (Supplementary Fig. 1). In

237   the 3D encoder module, there are three encoder blocks. Each block consists of two

238   3×3×3 convolutional layers followed by a leaky rectified linear unit (LeakyReLU) and

239   a 2×2×2 max pooling with strides of two in three dimensions. In the decoder module,

240   there are three decoder blocks, each of which contains two 3×3×3 convolutional layers

241   followed by a LeakyReLU and a 3D nearest interpolation. A group normalization[22]

242   layer is configured after each convolutional layer. The skip connections link low-level

243   features and high-level features by concatenating their feature maps. All operations

244   (convolutions, max poolings, and interpolations) in the network are in 3D to aggregate

245   spatial information and temporal information. For the loss function, we used the

246   arithmetic average of a L1-norm loss term and a L2-norm loss term. The model was

247   trained on 3D tiles with a spatial size of 64×64 pixels and a temporal size of 300 frames.

248   Small spatial size can lower memory requirements and reduce the training time, and

249   large temporal size is helpful to make full use of temporal information.

250   Adam optimizer[23] was used for network training with a learning rate of 0.00005 and

251   exponential decay rates of 0.5 for the first moment and 0.9 for the second moment. We

252   used Graphics Processing Units (GPU) to accelerate the training and test process. It

253   took about 12 hours to train our model for 20 epochs on a typical training set (about

254   1200 3D tiles) with a single GPU (Nvidia TITAN RTX, 24 GB memory). Training time

255   can be further shortened by using a more powerful GPU or parallelizing the training

256   process on multiple GPUs.

257   The full 3D architecture of DeepCAD makes it easy to overfit because 3D

258   convolutions usually involve more parameters than the 2D counterpart. The best

259   denoising performance is only achieved at the point where there is neither underfitting

260   nor overfitting. To screen out the model with the best generalization ability, we saved

261   the network snapshot after each training epoch and evaluated its performance on a

262   holdout validation set. We fed the validation data into each model and calculated the

263   standard deviation projection of the output stack of each model. Then, the average pixel

264   intensity was calculated on a small dark region (*e.g.* blood vessels or a small region

265   without neural activity during the recording) of all standard deviation projections. The

266   best model was selected to be the one with the smallest dark standard deviation.

267   **Data simulation.** Our simulation program includes a step for synthesizing the noise-

268   free video (ground truth) and a step for adding the Mixed Poisson-Gaussian (MPG)

269   noise (Supplementary Notes 1-2). Firstly, to generate realistic simulated calcium imaging

270   data, we constructed a neuron library containing the spatial profiles of 517 neurons.

271   These neurons were extracted using the constrained nonnegative matrix factorization

272   algorithm[21] (CNMF) from an experimentally obtained two-photon calcium imaging

273   data of a virus-transfected wild-type mouse expressing GCaMP6f (layer 2/3 at the

274   primary somatosensory cortex). For the spatial component that defines the location of

275   each neuron, 120 neurons were randomly selected from the library to keep the sparsity

276   of neurons. For the temporal component that defines the fluorescence fluctuations of

277   each neuron, MLspike[24] was employed to generate calcium traces with GCaMP6f

278   kinetics. Then, these two components were reshaped into 2D matrices and the simulated

279   noise-free data (1 μm/pixel spatial sampling rate, 30 Hz frame rate) was synthesized as

280   the product of the spatial matrix and the temporal matrix. The noise-contaminated

281   counterpart was ultimately generated by adding the content-related MPG noise. Data

282   with different imaging SNRs were simulated with different relative photon numbers.

283   Their relationship was investigated in Supplementary Fig. 7. All images were saved as

284   uncompressed tif files with the format of unsigned 16-bit integer (uint16). More details

285   of data simulation and related mathematical models are described in Supplementary

286   Notes 1-2.

287   **Single-neuron recordings.** The data of simultaneous two-photon imaging and

288   electrophysiological recordings of single-neuron activities were released by the

289   Svoboda lab[25] and were downloaded from the Collaborative Research in Computational

290   Neuroscience (CRCNS) platform. Only recordings of GCaMP6f neurons were used in

291   this study. The image stacks were fourfold downsampled to reduce the sampling rate

292   and some outlier recordings with very sparse spikes and low electrophysiological SNR

293   were excluded. Fluorescence traces were extracted from temporal stacks using

294 manually annotated cytoplasmic masks. For spike inference, we used the MLspike

295 algorithm[24], which was reported to rank first in the *Spikefinder* challenge[26]. All traces

296 were divided by their mean values for normalization before fed into the spike inference

297 pipeline. Recommended model parameters for GCaMP6f indicator were used to ensure

298 optimal performance of spike inference.

299 **Data analysis of neuronal populations.** Calcium imaging data of large neuronal

300 populations were first registered with a non-rigid motion correction method[27] and the

301 black edges of registered images were clipped. Then, CNMF[21] was employed as the

302 source extraction method for neuron segmentation and trace extraction. A spatial matrix

303 and a temporal matrix can be obtained from each video, storing the spatial footprints

304 and corresponding calcium traces of all active neurons, respectively. The same set of

305 parameters was used for the original low-SNR recording and corresponding DeepCAD

306 enhanced counterpart, as well as the high-SNR recording. Simulated data were analyzed

307 following the same pipeline except motion correction. Along with automatic neuron

308 extraction, we also performed manual annotations to inspect our results. High-SNR

309 recordings were tenfold downsampled along the time axis by averaging each

310 consecutive ten frames, which reduced the disturbance of detection noise and was

311 helpful to improve annotation accuracy. Boundaries of all active components were

312 annotated using the ROI Manager toolbox of Fiji. The final segmentation masks were

313 generated through subsequent morphological operations of images and connected

314 domain extraction implemented with customized MATLAB scripts.

315 **Performance metrics.** Two types of metrics were used for quantitative evaluation of

316 the spatial and temporal performance of DeepCAD. For synthetic calcium imaging data,

317 corresponding clean images and ground-truth calcium traces were available. SNR and

318 PSNR were used as the spatial metric to evaluate pixel-level similarity between

319 DeepCAD enhanced images and ground-truth images. Pearson correlation coefficient

320 (R) was used as the temporal metric to reflect the similarity between enhanced traces

321 and ground-truth traces. The Pearson correlation between signal x and the reference

322 signal y is defined as

323
$$R = \frac{\mathrm{E}[(x - \mu_x)(y - \mu_y)]}{\sigma_x \sigma_y}$$

324 where μ_x and μ_y are the mean values of signal x and y, respectively; σ_x and σ_y are the

325 standard deviations of signal x and y, respectively; E represents arithmetic mean.

326 Furthermore, we also evaluated the performance of DeepCAD based on more

327 complex downstream tasks such as neuron extraction and spike inference, which are

328 the most crucial prerequisites in functional analysis of neural circuits from calcium

329 imaging data. We considered neuron extraction as an instance segmentation problem

330 and adopted an object-level metric to evaluate segmentation performance[28]. Different

331 intersection-over-union (IoU, defined as the intersection area divided by the union area

332 of two objects) thresholds were selected to determine correctly segmented objects. For

333 a specified IoU threshold, the segmentation accuracy (F1 score) was defined as the

334 harmonic mean of sensitivity and precision, which can be formulated as

335
$$F1 = \frac{2TP}{2TP + FP + FN}.$$

336 Here, TP, FP, and FN are the number of true positives, false positives, and false

337 negatives, respectively. When applied CNMF as the source extraction method, the SNR

338 of calcium traces was quantified with the peak SNR automatically calculated by the

339 CaImAn toolbox[29] with infinite outliers eliminated. For spike inference, we used the

340 error rate (ER) to quantify the performance of spike inference, which is defined as ER

341 = 1- F1. Spikes detected from simultaneous electrophysiological recordings were used

342 as the ground truth for ER calculation. The evaluation process was implemented with

343 customized MATLAB scripts. SNR, PSNR, Pearson correlation coefficient, and IoU

344 were computed using built-in functions.

345 ## Data availability

346 Our data will be made publicly available post peer-review.

347 ## Code availability

348 Our python code and Fiji plugin will be made publicly available post peer-review.

349 ## Acknowledgements

350 We would like to acknowledge Y. Tang and Y. Yang at the School of Medicine of Tsinghua

351 University for providing transgenic mice for imaging and the mesoscope imaging data for

352 cross-system validation. We thank the Svoboda lab at Janelia Research Campus for releasing

357   **Author Contributions**

358   Q. D., H. W., L. F. and XY. L. conceived this project. Q. D., H. W. and L. F. supervised this

359   research. XY. L. and G. Z. designed detailed implementations and processed the data. XY. L

360   designed and set up the imaging system. XY. L and G. Z. conducted the experiments. G. Z.

361   developed the python code and the Fiji plugin. J. W., Y. Z., and X. L. directed the experiments

362   and data analysis. L. F., Y. Z., Z. Z, H. Q. and H. X. gave critical support on system setup and

363   imaging procedure. J. W., L. F., Y. Z., X. L., H. Q., H. X., H. W. and Q. D. gave critical

364   discussions on the results. All authors participated in the writing of the paper.

References

1. Grienberger, C. & Konnerth, A. Imaging Calcium in Neurons. *Neuron* **73**, 862-885 (2012).
2. Lu, R. et al. Video-rate volumetric functional imaging of the brain at synaptic resolution. *Nat. Neurosci.* **20**, 620-628 (2017).
3. Weisenburger, S. et al. Volumetric Ca(2+) Imaging in the Mouse Brain Using Hybrid Multiplexed Sculpted Light Microscopy. *Cell* **177**, 1050-1066 e1014 (2019).
4. Chow, D.M. et al. Deep three-photon imaging of the brain in intact adult zebrafish. *Nat. Methods* **17**, 605-608 (2020).
5. Calarco, J.A. & Samuel, A.D. Imaging whole nervous systems: insights into behavior from worms to fish. *Nat. methods* **16**, 14-15 (2019).
6. Sabatini, B.L., Oertner, T.G. & Svoboda, K. The Life Cycle of Ca2+ Ions in Dendritic Spines. *Neuron* **33**, 439-452 (2002).
7. Chen, T.W. et al. Ultrasensitive fluorescent proteins for imaging neuronal activity. *Nature* **499**, 295-300 (2013).
8. Ji, N., Freeman, J. & Smith, S.L. Technologies for imaging neural activity in large volumes. *Nat. Neurosci.* **19**, 1154-1164 (2016).
9. Svoboda, K. & Yasuda, R. Principles of two-photon excitation microscopy and its applications to neuroscience. *Neuron* **50**, 823-839 (2006).
10. Skylaki, S., Hilsenbeck, O. & Schroeder, T. Challenges in long-term imaging and quantification of single-cell dynamics. *Nat. Biotechnol.* **34**, 1137-1144 (2016).
11. Podgorski, K. & Ranganathan, G. Brain heating induced by near-infrared lasers during multiphoton microscopy. *J. Neurophysiol.* **116**, 1012-1023 (2016).
12. Wang, T. et al. Quantitative analysis of 1300-nm three-photon calcium imaging in the mouse brain. *eLife* **9** (2020).
13. Dana, H. et al. High-performance calcium sensors for imaging activity in neuronal populations and microcompartments. *Nat. Methods* **16**, 649-657 (2019).
14. Samantaray, N., Ruo-Berchera, I., Meda, A. & Genovese, M. Realization of the first sub-shot-noise wide field microscope. *Light Sci. Appl.* **6**, e17005 (2017).
15. Weigert, M. et al. Content-aware image restoration: pushing the limits of fluorescence microscopy. *Nat. Methods* **15**, 1090-1097 (2018).
16. Belthangady, C. & Royer, L.A. Applications, promises, and pitfalls of deep learning for fluorescence image reconstruction. *Nat. Methods* **16**, 1215-1225 (2019).
17. Wang, H. et al. Deep learning enables cross-modality super-resolution in fluorescence microscopy. *Nat. Methods* **16**, 103-110 (2019).
18. Ouyang, W. et al. Deep learning massively accelerates super-resolution localization microscopy. *Nat. Biotechnol.* **36**, 460-468 (2018).

19. Lehtinen, J. et al. Noise2Noise: Learning Image Restoration without Clean Data. In *Proc. 35th International Conference on Machine Learning* (eds Dy, J. & Krause, A.) 2965–2974 (PMLR, 2018).

20. Çiçek, Ö. et al. 3D U-Net: learning dense volumetric segmentation from sparse annotation. In *Medical Image Computing and Computer-Assisted Intervention* 424–432 (2016).

21. Pnevmatikakis, E.A. et al. Simultaneous Denoising, Deconvolution, and Demixing of Calcium Imaging Data. *Neuron* **89**, 285-299 (2016).

22. Wu, Y. & He, K. Group normalization. In *2018 IEEE European Conference on Computer Vision* (ECCV) 3–19 (IEEE, 2018).

23. Kingma, D. P. & Ba, J. L. Adam: a method for stochastic optimization. In *International Conference on Learning Representations* 1–15 (2015).

24. Deneux, T. et al. Accurate spike estimation from noisy calcium signals for ultrafast three-dimensional imaging of large neuronal populations in vivo. *Nat. Commun.* **7**, 12190 (2016).

25. GENIE project, Janelia Farm Campus, HHMI; Karel Svoboda (contact). (2015). Simultaneous imaging and loose-seal cell-attached electrical recordings from neurons expressing a variety of genetically encoded calcium indicators. CRCNS.org. http://dx.doi.org/10.6080/K02R3PMN

26. Berens, P. et al. Community-based benchmarking improves spike rate inference from two-photon calcium imaging data. *PLoS Comput. Biol.* **14**, e1006157 (2018).

27. Pnevmatikakis, E.A. & Giovannucci, A. NoRMCorre: An online algorithm for piecewise rigid motion correction of calcium imaging data. *J. Neurosci. Methods* **291**, 83-94 (2017).

28. Caicedo, J.C. et al. Nucleus segmentation across imaging experiments: the 2018 Data Science Bowl. *Nat. Methods* **16**, 1247-1253 (2019).

29. Giovannucci, A. et al. CaImAn an open source tool for scalable calcium imaging data analysis. *eLife* **8** (2019).
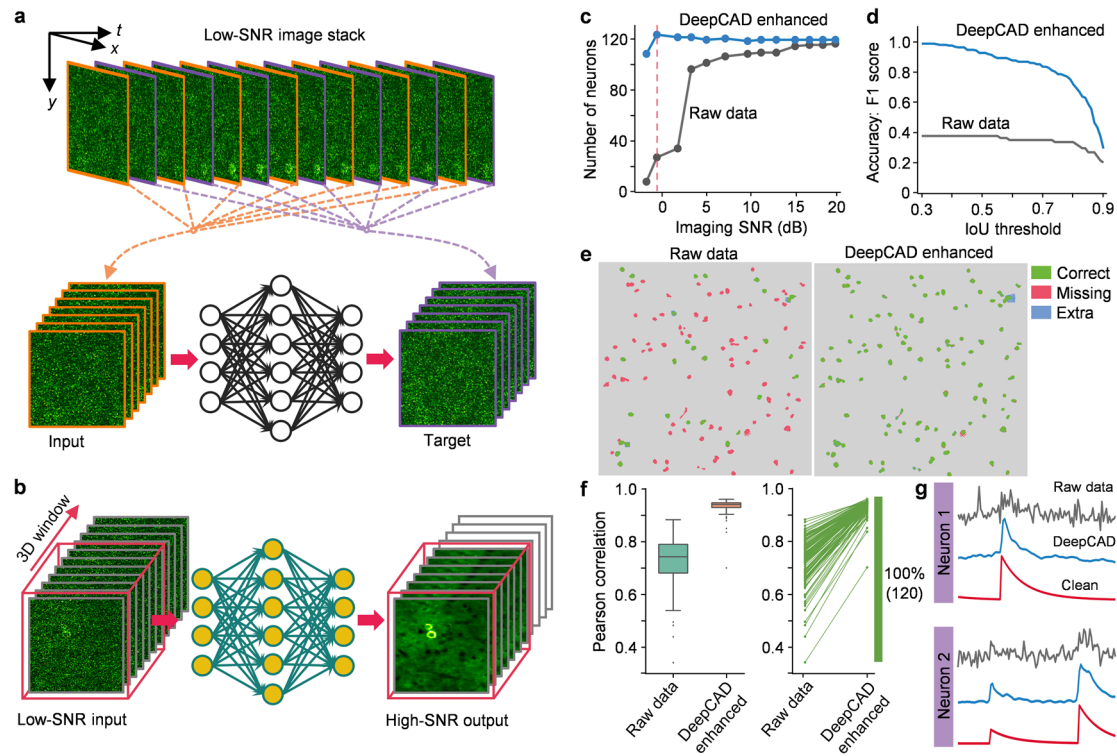
Fig. 1 | General principle and validation of DeepCAD. a, Self-supervised training strategy of DeepCAD. Consecutive frames in the original low-SNR stack are divided into two sub-stacks, used as the input volume and corresponding target volume to train a deep neural network (3D U-Net). After training, a denoising model can be established and memorized in network parameters. **b**, Application of the DeepCAD model. For subsequent acquisitions, a 3D (*x-y-t*) window traverses the entire stack and 3D tiles are sequentially fed into the pre-trained model. Denoised recordings will be obtained after the processing of the model. **c**, The number of neurons extracted under different imaging SNRs before and after the enhancement of DeepCAD. N=120 active neurons were simulated in the field of view (FOV). **d**, Accuracy of neuron segmentation quantified with F1 score at different intersection-over-union (IoU) thresholds (imaging SNR=-0.7 dB, indicated by the red dashed line in **c**). **e**, Spatial profiles of extracted neurons (imaging SNR=-0.7 dB). Correctly segmented regions (true positive) are colored green. Missing (false negative) and extra regions (false positive) are colored red and blue, respectively. Neuron extraction was implemented with CNMF[21]. **f**, Left: boxplot showing the distribution of Pearson correlation coefficients with clean traces before and after denoising (N=120). Right: increases of trace correlations. Each line represents one of 120 calcium traces and correlation coefficients of all neurons were observed improved. **g**, Calcium transients indiscernible from noise (gray) can be restored by DeepCAD (blue). Traces without noise contamination (red) serve as the ground truth for comparison.
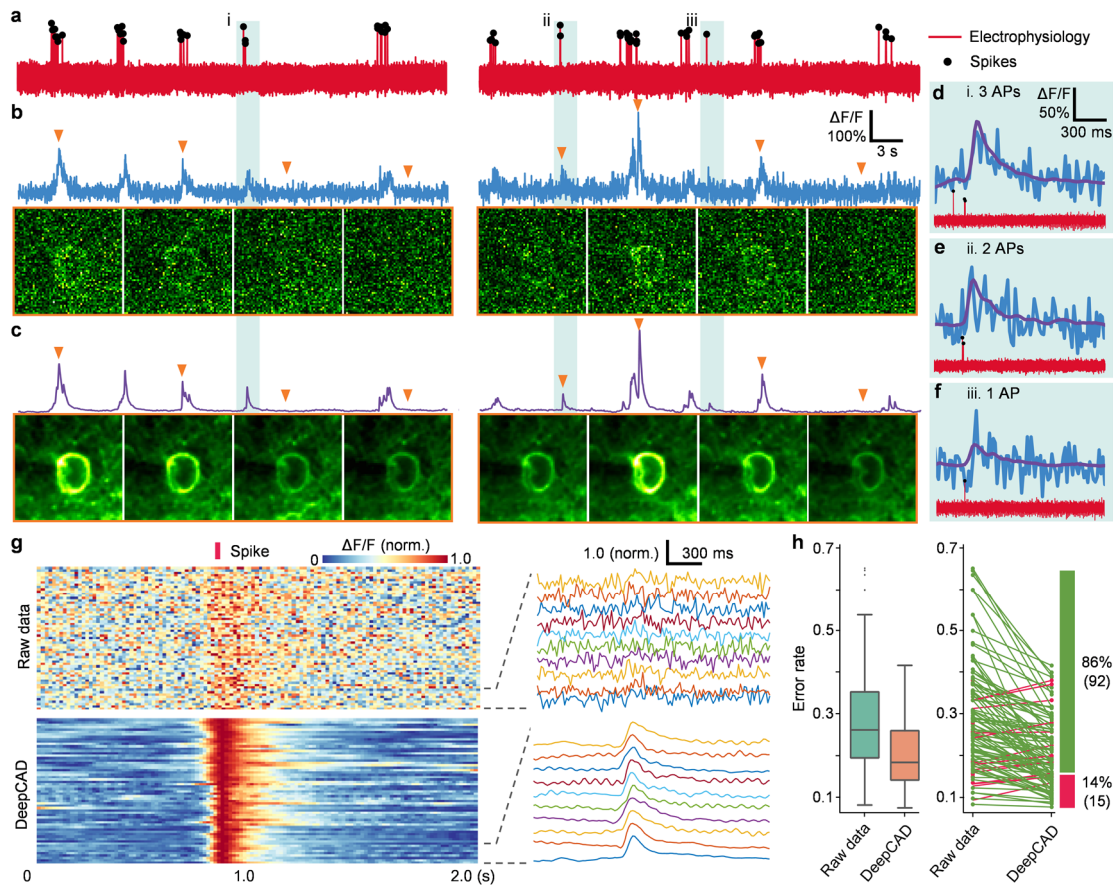
457

Fig. 2 | Spatiotemporal enhancement of DeepCAD. a, Electrophysiological recordings of neural activities from a single neuron. Detected spikes are marked with black dots. **b,** Two-photon calcium imaging of the same neuron synchronized with cell-attached electrophysiology. Both spatial footprints and temporal traces of the neuron were severely corrupted in detection noise. Representative frames indicated with orange triangles are presented below the trace. **c,** Fluorescence traces and representative frames after the enhancement of DeepCAD. **d-f,** The most imperceptible calcium transients evoked by three APs (**d**), two APs (**e**), and one AP (**f**) can be resolved and still keep their original dynamics noise removal. **g,** Calcium fluctuations evoked by 61 isolated action potentials. All spikes were normalized and temporally aligned with the red bar. Zoom-in traces are shown in the right panel. **h,** Left: Boxplot showing the distribution of error rates (lower is better) of spike inference for calcium traces extracted from enhanced data compared with those extracted from the original data (N=107). Real spike timings were revealed by simultaneous cell-attached recordings. Right: decreases of the error rate of spike inference. Each line represents one of 107 recordings, using green for decreased error rates and red for increased error rates.
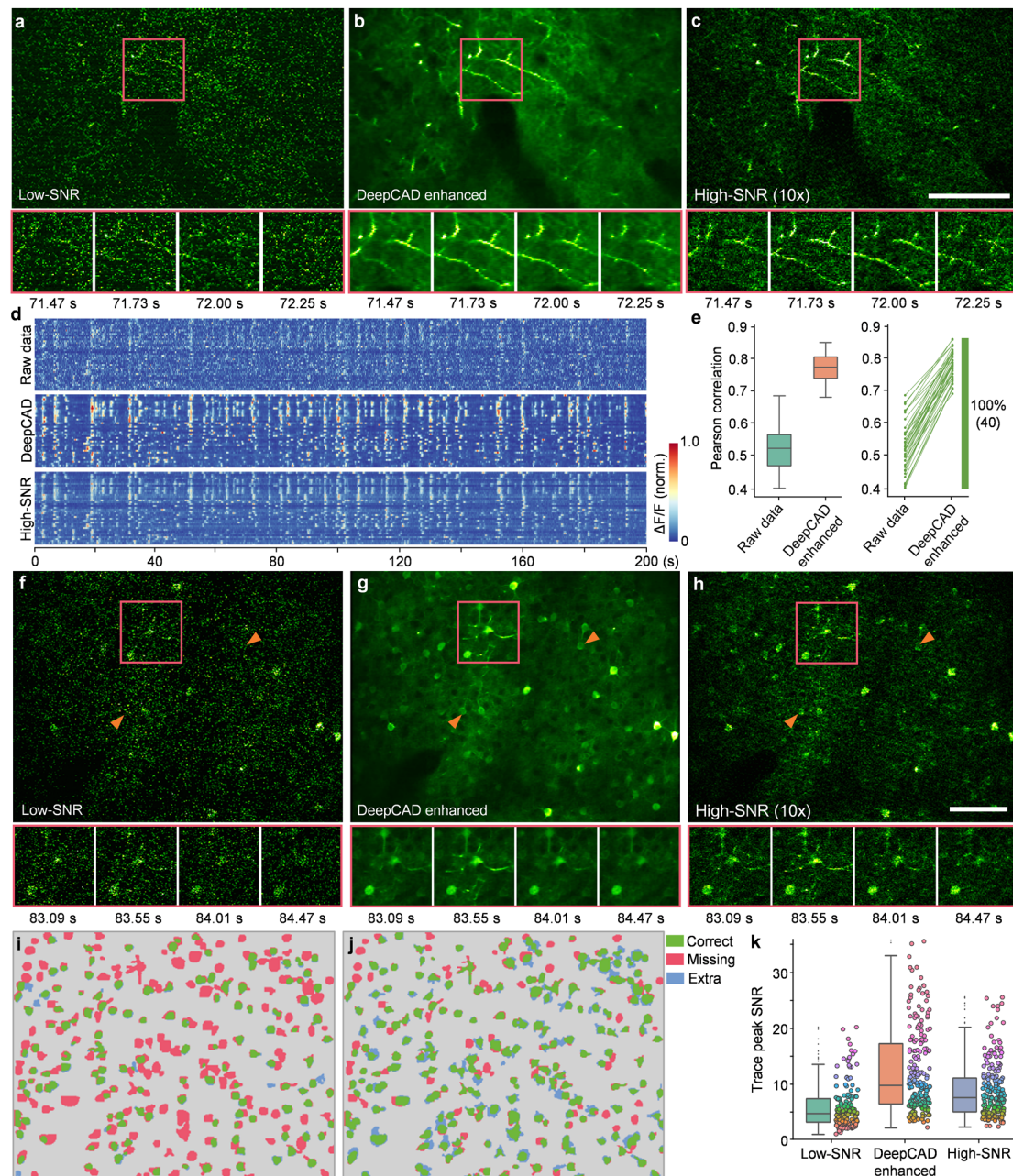
474

Fig. 3 | DeepCAD reinforces the recording of large neuronal populations. a, Spontaneous neuropil activities in layer 1 of the mouse cortex captured by the low-SNR detection path. **b**, Images restored from the low-SNR recording using DeepCAD. **c**, Synchronized recording acquired by the high-SNR detection path (10-fold imaging SNR). Magnified views of the boxed regions show calcium transients in a ~0.8 s time window. Scale bar 100 μm. **d**, Fluorescence traces extracted from 40 dendritic pixels. Top: low-SNR recording, Middle: DeepCAD enhanced recording, Bottom: high-SNR recording. **e**, Pearson correlation coefficients of single-pixel calcium traces before and after denoising (left). High-SNR traces were used as the reference for correlation calculation. Improvements were observed in all 40 traces (right). **f**, Low-SNR recording of somatic signals in cortical layer 2/3. **g**, DeepCAD enhanced recording. **h**, Synchronized high-SNR recording (10-fold imaging SNR). Orange arrows point to two

487   neurons. Magnified views of the boxed regions show calcium transients in a ~1.4 s time

488   window. Scale bar 100 μm. **i**, Neurons extracted from the original low-SNR recording

489   (N=150). **j**, Neurons extracted from the DeepCAD enhanced recording (N=229).

490   Manual annotations served as the ground truth. Correctly segmented regions (true

491   positive) are colored green. Missing (false negative) and extra regions (false positive)

492   are colored red and blue, respectively. **k**, Distribution of peak SNRs of extracted

493   calcium traces. CNMF was used for source extraction and peak SNR estimation.